A dendrite-free composite Li metal anode enabled by lithiophilic Co, N codoped porous carbon nanofibers

Chengcheng Zhao [a], Shiyun Xiong [b], Huilan Li [a], Zhuhong Li [b], Chu Qi [a], Hao Yang [a], Lina Wang [a,*], Yu Zhao [b,**], Tianxi Liu [a,c,***]

[a] State Key Laboratory for Modification of Chemical Fibers and Polymer Materials, College of Materials Science and Engineering, Innovation Center for Textile Science and Technology, Donghua University, Shanghai, 201620, China
[b] Institute of Functional Nano and Soft Materials (FUNSOM), Jiangsu Key Laboratory for Carbon-Based Functional Materials and Devices, Soochow University, Jiangsu, 215123, China
[c] Key Laboratory of Synthetic and Biological Colloids, Ministry of Education, School of Chemical and Material Engineering, Jiangnan University, Wuxi, 214122, China

HIGHLIGHTS

- A lithiophilic composite anode is enabled by Co/N codoped carbon nanofibers (CNF).
- The Co/N is derived from metal-organic frameworks (MOFs) self-assembled on CNF.
- A highly porous structure is readily created in the CNF from pyrolysis of the MOFs.
- The synergistic effect between Co and N defects leads to enriched Li affinity.
- The pores in CNF act as buffer space for volume variation on Li plating/ stripping.

GRAPHICAL ABSTRACT
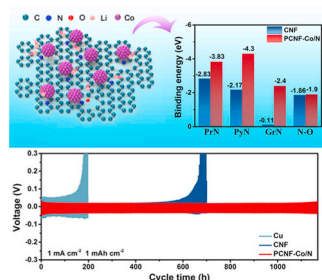
ARTICLE INFO

ABSTRACT

Lithium (Li) metal is the most promising anode material for the next-generation high-energy density battery due to its high specific capacity and low redox potential. However, its practical applications is challenged by uncontrolled Li dendrite growth and volume expansion. In this work, we propose a cobalt-enhanced nitrogen doped porous carbon nanofibers (PCNF–Co/N) with an enhanced lithiophilic property. The Co/N co-doping is achieved through pyrolysis of self-assembled Co/Zn metal-organic framework (MOF) nanosheets on carbon nanofibers (CNF). The synergistic effect between the simultaneously introduced Co and N defects not only boosts the Li affinity of pyridinic and pyrrolic N but also transfers the graphitic N into lithiophilic, providing crucial roles for uniform plating of Li. Meanwhile, the porous structure formed by Zn sublimation provides sufficient buffer space for internal stress caused by Li plating/stripping. As a result, the PCNF–Co/N@Li anode delivers a long lifespan

* Corresponding author.
** Corresponding author.
*** Corresponding author. State Key Laboratory for Modification of Chemical Fibers and Polymer Materials, College of Materials Science and Engineering, Innovation Center for Textile Science and Technology, Donghua University, Shanghai, 201620, China.
E-mail addresses: linawang@dhu.edu.cn (L. Wang), yuzhao@suda.edu.cn (Y. Zhao), txliu@dhu.edu.cn (T. Liu).

over 1400 h with a low voltage hysteresis. When paired with a LiFePO₄ cathode, the full cell demonstrates decent cyclic stability and rate capability, demonstrating the capability of PCNF–Co/N in developing composite Li-metal anode with enhanced lithiophilicity and low internal stress.

1. Introduction

Lithium-ion (Li-ion) batteries are approaching a bottleneck mainly due to the limited capacity of cathodes and the most widely used graphite anode (370 mAh g^{-1}). Li metal is a promising anode material due to its theoretical capacity of 3860 mAh g^{-1} that is over ten times higher than conventional anode based on graphite, and the most negative electrochemical potential of -3.04 V vs SHE [1–4]. However, uncontrolled Li dendrite growth caused by uneven ion distribution and infinite volume expansion during the plating/stripping process not only results in inevitable capacity loss but also brings in severe safety risk [5–7].

Much effort has been made for the successful implementation of Li metal. One plausible approach is to construct a stabilized solid electrolyte interphase (SEI) on the Li-anode surface [8,9]. Various electrolyte modifications have been applied to enhance the mechanical strength and chemical stability of the autogenetic SEI layer, such as halogenated salt [10], copper fluoride [11] and so forth. The building of an artificial SEI layer is another approach to accommodate the dendrite formation. For example, Shen et al. fabricated a hydrophobic graphite fluoride–lithium fluoride SEI on Li-metal anode [12]. And Li et al. coated the Li$_{6.4}$La$_3$Zr$_{1.4}$Ta$_{0.6}$O$_{12}$ particles on Cu foam to build a SEI [13]. In spite of the improved Li plating/stripping performance, due to the intrinsic "hostless" property of Li metal, the large volume change would cause significant internal stress accumulation and thereby crumble the SEI layer upon repeating cycling [14–17].

Alternatively, storing Li into favorable constructions holds the promise to regulate the Li$^+$-ion distribution as well as to buffer the volume change [5,18–21]. A series of hosts including carbon- or graphene-based materials [14,22–26] and copper/nickel foams [15, 27–29] have been extensively examined. However, the lack of regular nucleation sites makes such hosts less effective in uniform Li plating under high current density. Later efforts have focused on surface engineering of skeletons with precious metals or polar atoms to improve Li affinity. For metals, Ke et al. have coated lithiophilic AuLi$_3$ particles on the lithiophobic Ni foam so that the nucleation energy barrier can be reduced [29]. Xue et al. have assembled continuous silver nanowires on a porous graphene skeleton to improve Li-plating at high rates [30]. Li et al. have introduced a cobalt/Li$_2$O fibrous framework that is able to provide adequate Li nucleation sites [31]. For polar heteroatoms, Wang et al. have suggested that sulfur doped graphene could increase the lithium adsorption for the overall surface with a mild gradient [32]. Zhang et al. have demonstrated that the nitrogen-containing functional groups, especially pyridinic nitrogen (PyN) and pyrrolic nitrogen (PrN), showed strong binding energy with Li [24]. However, the graphitic nitrogen (GrN) with lithiophobic nature actually occupies a dominant proportion among the introduced nitrogen-containing functional groups. In addition, fabrication of a flexible host with effective composite lithiophilic sites still remains challenging.

Herein, we demonstrate a strategy by using an in-situ growth method to realize cobalt-enhanced nitrogen doped porous carbon nanofibers (PCNF–Co/N) with greatly enhanced lithiophilic property. The Co and partial N atoms are derived from bimetallic 2-methylimidazole (C$_8$H$_{10}$N$_4$Co$_{2/3}$Zn$_{1/3}$) metal-organic framework (MOF) nanosheets, which are self-assembled in solution onto flexible carbon nanofibers (CNF) prepared through an electrospun method. A highly porous structure is readily created in the CNF from volatility of metal Zn in the carbonized MOF during a high-temperature annealing process. The interconnected conductive carbon framework makes the electrolyte kinetically accessible to the nanofibers via fast charge transfer. And its

porous nature acts as abundant buffer space for volume variation upon Li plating/stripping. More importantly, the synergistic effect between Co and N defects not only boosts the Li affinity of PrN and PyN, but also transfers the lithiophobic GrN into lithiophilic. As a result, a symmetrical composite Li-metal cell keeps stable over 1400 h with low voltage hysteresis ca. 4 mV at 0.5 mA cm^{-2}, 1.0 mAh cm^{-2}. When paired with a LiFePO₄ cathode, the full cell delivers a reversible capacity of 108.7 mAh g^{-1} after 500 cycles at 1 C (1 C = 170 mA g^{-1}) with a capacity decay of only 0.02% per cycle. This strategy demonstrates an effective solution to regulate Li$^+$-ion distribution with control over both position and volume change.

2. Experimental section

2.1. Material synthesis

Preparation of CNF: The carbon nanofiber film was prepared via an electrospinning technique on electrospinning setup (ET-2531, Beijing Yongkangleye Co., LTD). Typically, the solution of 9.0 g of *N,N*-dimethylformamide (DMF, 99.5%, Shanghai Lingfeng Chemical) with pre-dissolved 0.25 g polymethyl methacrylate (PMMA, Mw = 120 000, Sigma-Aldrich) was prepared firstly. Then, 0.75 g of polyacrylonitrile (PAN, Mw = 15 000, Sigma-Aldrich) was added into the solution and stirred for 12 h to obtain a clear solution. The solution was inhaled into an injector (5 mL), the electrospinning voltage was 8–14 kV, and the feeding rate was 0.08 mm min^{-1}, the distance between the needle and the receiving roller was 23.0 cm. After dried under 60 °C for 12 h in a vacuum oven to remove abundant solvent, the obtained electrospun film was placed into a tube furnace at 280 °C for 3 h in air and then carbonized at 1000 °C in Ar.

Preparation of PCNF–Co/N: Co(NO$_3$)$_2$·6H$_2$O (≥98.5%, Sinopharm) and Zn(NO$_3$)$_2$·6H$_2$O (≥99%, Sinopharm) in a mole ratio of 2:1 were dissolved in deionized water to form a solution, and 2-methylimidazole (99%, Sinopharm) was dissolved into deionized water to form another solution. The two solutions were stirred for 1 h and then quickly blended together. Subsequently, a piece of as-prepared CNF film that pre-treated with plasma was immersed in the blended solution and kept still for 24 h. For the plasma treatment, the CNF was treated with vacuum plasma using a Tonson TS-PL02 plasma etching system (vacuum atmosphere, 400 W power density for 10 min). Then, the as-obtained MOF-decorated CNF film (denoted as CNF@MOF) was washed by deionized water and ethanol thoroughly and dried in a vacuum oven at 60 °C for 12 h. Finally, the CNF@MOF was annealed at 950 °C in Ar for 3 h to obtain the PCNF–Co/N.

2.2. Material characterizations

The morphological characterizations were performed by a field emission scanning electron microscope (SEM, 7500F, JEOL) and transmission electron microscope (TEM, JEM-2100F, JEOL) combined with Energy-dispersive X-ray spectroscopy (EDS). For handling the electrodes at different states of discharge-charge, the electrodes were taken from the cells, washed by 1, 2-dimethoxyethane (DME, ≥99%, Sigma-Aldrich) and dried in the glove box for 24 h before the morphological measurements. X-ray diffraction (XRD) patterns were obtained using an X-ray diffractometer (D/max-2500VB+/PC, Rigalcu) equipped with Cu Kα radiation. The nitrogen sorption/desorption measurements were conducted on a Quadrasorb adsorption instrument (Quantachrome Instruments). And the specific surface area was calculated according to the multipoint Brunauer–Emmett–Teller (BET) method. Raman spectra
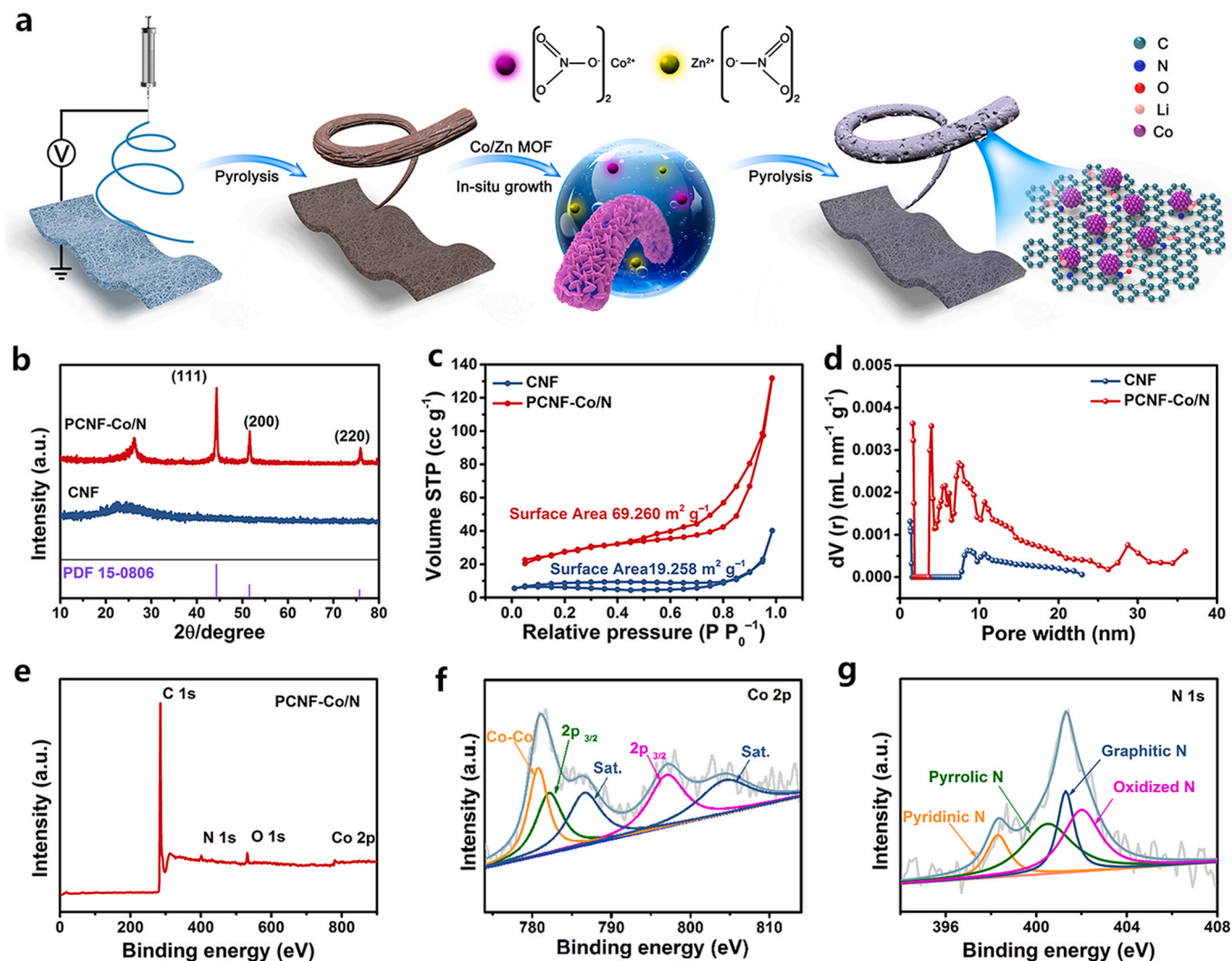
Fig. 1. (a) Schematic illustration for synthetic procedure of PCNF–Co/N. (b) XRD patterns, (c) N_2 sorption isotherms and (d) Pore width distribution of CNF and PCNF–Co/N. (e) XPS survey, (f) Co 2p, and (g) N 1s core level spectra of PCNF–Co/N.

were collected from an inVia Reflex Raman Spectrometer (532 nm, inVia-Reflex, Renishaw). X–ray photoelectron spectroscopy (XPS) analyses were performed on a spectrometer (Escalab 250Xi) with Al Kα X-ray radiation. Thermogravimetric analysis (TGA) was conducted on a TG-DSC analyzer (NETZSCH TG 209 F1 Libra) in the temperature range from ambient to 1000 °C in Ar atmosphere. Inductively coupled plasma (ICP) analysis was conducted on Plasma spectrometer (Prodigy-ICP).

2.3. Electrochemical measurements

CR2025 coin cells were assembled in an argon-filled glove box (<1 ppm of H_2O and O_2, Mikrouna) to investigate the electrochemical performance. For symmetric cell test, a Cu@Li, CNF@Li or PCNF–Co/N@Li composite anode (12 mm in diameter) was as the working electrode, which was pre-deposited with 10 mAh cm^{-2} of Li at 0.5 mA cm^{-2}. Li metal foil was used as a counter/reference electrode for symmetric cell test. For the pre-deposition step, the cell with Cu, CNF or PCNF–Co/N working electrode and fresh Li foil counter electrode were initial discharge at 0.5 mA cm^{-2} for 20 h. The polypropylene/polyethylene microporous membrane (Celgard 2325) was used as the separator. The electrolyte was 1 M lithium bis (trifluoromethanesulfonyl) imide (LiTFSI) and 0.2 M lithium nitrate (LiNO$_3$) in 1, 3-dioxolane (DOL)/1, 2-dimethoxyethane (DME) (1/1, v/v) (Shanghai Songjingenergy Co., LTD). The galvanostatic tests were performed on a LAND battery test

system (Wuhan, China) at room temperature. Cyclic voltammetry (CV) tests were performed on an electrochemical workstation (Arbin Instruments, USA) between −0.5 V and 3.2 V (vs Li/Li$^+$). The Electrochemical impedance spectroscopy (EIS) measurements were recorded on a CHI660E electrochemical workstation (Shanghai Chenhua, China) in a frequency range from 0.1 Hz to 100 kHz at a potentiostatic signal amplitude of 5 mV.

For full cell test, a Cu@Li, CNF@Li or PCNF–Co/N@Li composite was used as the anode, LiFePO$_4$ was used as the cathode. For the deposition of Li on Cu, CNF and PCNF–Co/N, CR2025 coin cells were fabricated using the Cu, CNF and PCNF–Co/N as working electrode and Li foil as counter electrode. After discharged at 0.5 mA cm^{-2} for 20 h, which corresponding to 10 mAh cm^{-2} of lithium, the cells were disassembled in glove box and the electrode was washed with DME for three times. After dried for 24 h, the as-prepared composite anode was directly used to pair with LiFePO$_4$ for full cell test. To prepare the LiFePO$_4$ cathode, a black viscous slurry consisting of LiFePO$_4$ (Shenzhen Dynanonic Co. LTD), carbon black (Acetylene, 99.9%, Alfa Aescar), and poly (vinylidene fluoride) (PVdF, HSV900) in a weight ratio of 90:5:5 dispersed in *N*-methyl-2-pyrrolidone (NMP, ≥99.0%, Shanghai Lingfeng Chemical) was blade-casted onto Al foil. The electrode was dried in vacuum at 80 °C for 4 h and then increased to 120 °C for 8 h before to be punched into disks with a diameter of 12.0 mm. The LiFePO$_4$ loading of the cathode is ca. 5 mg cm^{-2}. The CR2025 coin cells with Cu@Li,
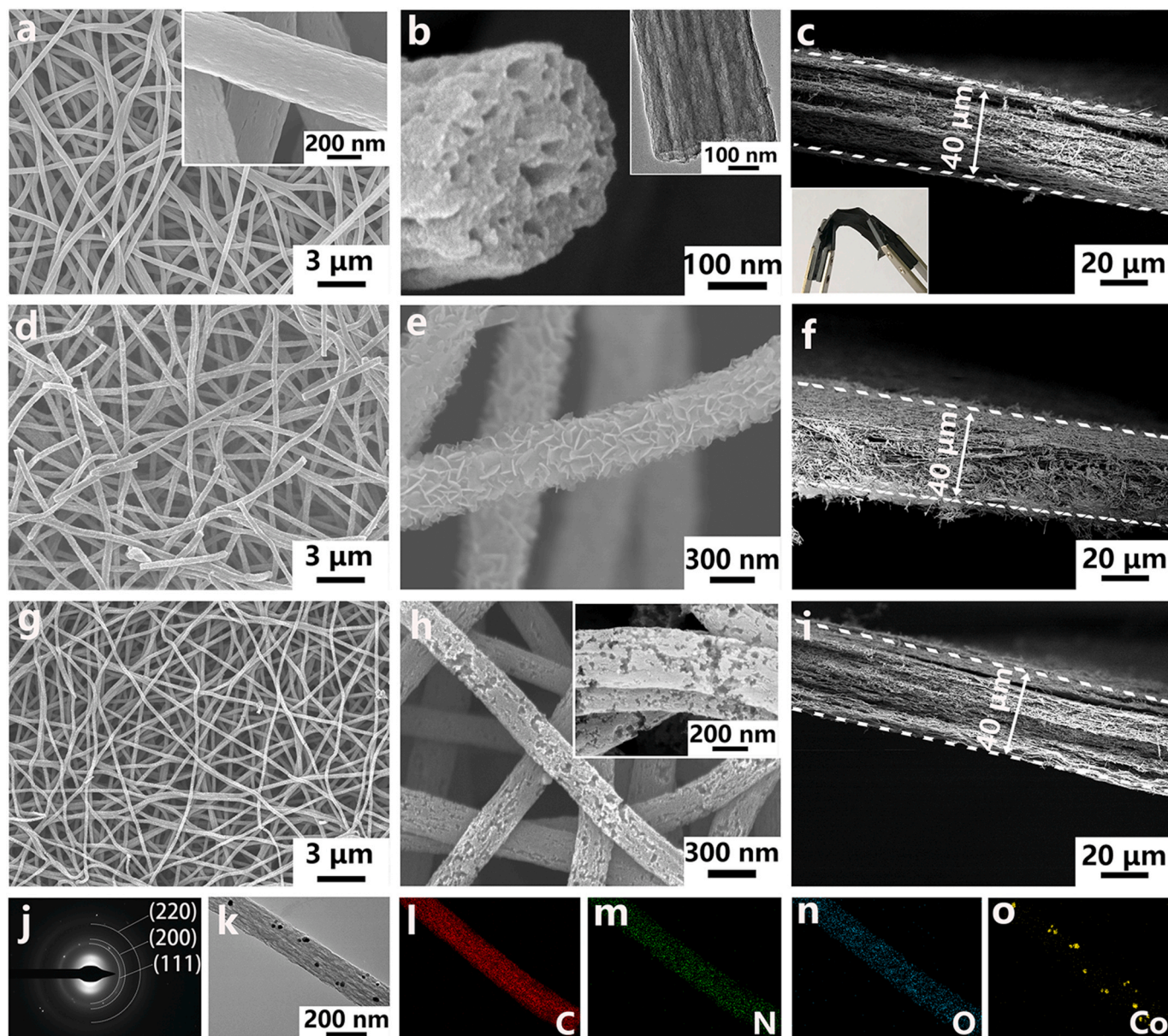
Fig. 2. SEM images of (a–c) CNF, (d–f) CNF@MOF, (g–i) PCNF–Co/N. The inset white boxes of (a) and (h) are high magnifications. The inset white box of (b) is TEM image of single CNF. The inset white box of (c) is the digital photo of CNF. (c, f, i) is the cross-sectional images of the overall films. (j) SAED image of Co. (k–o) TEM image of PCNF–Co/N and corresponding elemental mapping of C, N, O and Co.

CNF@Li or PCNF–Co/N@Li composite anode (12 mm in diameter) and LiFePO$_4$ cathode was assembled in a glove box. The electrolyte was 1.0 M LiPF$_6$ dissolved in ethylene/dimethyl carbonate/diethyl carbonate (EC/DMC/DEC, 1:1:1, v/v/v) (Shanghai Songjingenergy Co., LTD). The amount of the electrolyte used in each cell is 60 μL. The cells were galvanostatically cycled at 0.2, 0.5, 1, 2, 5 and 10 C (1 C = 170 mAh g^{-1}), respectively with a cut-off voltage of 2.0–4.0 V (vs Li/Li$^+$).

2.4. Calculation method

All structures were optimized with Gaussian 09 software [33] at the B3LYP/6–31 + g(d) level of theory. The Li binding energy of all structures was calculated as E(A + Li)-E(A)-E(Li), where E(A + Li) means the energy of the structure attached with Li, while E(A) and E(Li) correspond to the energy without attaching Li atom and the energy of Li atom, respectively. The charge density difference of all structures was obtained by subtracting the charge density of the structure without Li and of a single Li from the charge density of the combined structure. The calculation of charge density difference was carried out with Multiwfn [34] based on the wavefunctions obtained by Gaussian 09.

3. Results and discussion

3.1. Synthesis and characterizations of PCNF–Co/N

The synthetic procedure of PCNF–Co/N is schematically shown in Fig. 1a. In brief, the electrospun precursor film was firstly prepared from a DMF solution containing PAN and PMMA. Then, the as-spun film was dried and thermally treated in Ar flow to obtain a flexible and free-standing CNF film. During the heating process, the PAN was carbonized in 250–400 °C and the PMMA was simultaneously removed by sublimation (Fig. S1a) [35]. Afterwards, the obtained CNF film was immersed into a blended solution of Co(NO$_3$)$_2$·6H$_2$O, Zn(NO$_3$)$_2$·6H$_2$O and 2-methylimidazole. C$_8$H$_{10}$N$_4$Co$_{2/3}$Zn$_{1/3}$ MOF were self-assembled onto the CNF
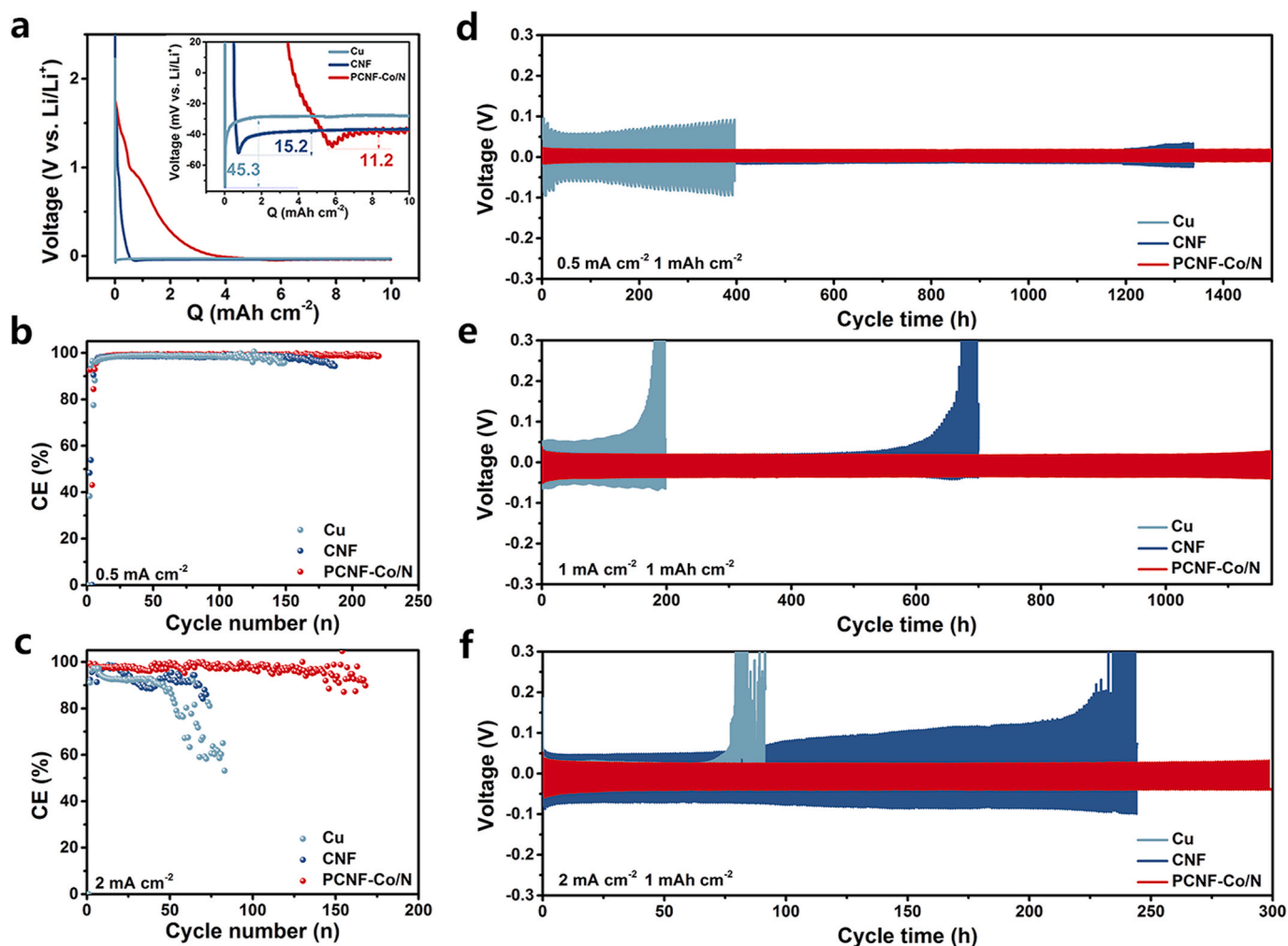
Fig. 3. (a) Nucleation overpotential of Cu, CNF and PCNF–Co/N electrode at 0.5 mA cm^{-2}. (b) CE of Cu‖Li, CNF‖Li and PCNF–Co/N‖Li cells at 0.5 mA cm^{-2} and (c) 2 mA cm^{-2} (d–f) Galvanostatic cycling performance of symmetric cell with different electrodes at different current densities (d) 0.5 mA cm^{-2}, (e) 1 mA cm^{-2} and (f) 2 mA cm^{-2}. The capacity was limited to 1 mAh cm^{-2}.

after 24 h (Fig. S2a). Finally, the as-prepared CNF@MOF was treated at 950 °C in Ar to obtain the PCNF–Co/N. During this process, the CNF is highly stable (Fig. S1b) and the MOFs are pyrolyzed. A distinct color change was observed from black (CNF) to purple (CNF@MOF) and finally to black gray PCNF–Co/N film (Fig. S2b).

XRD was used to reveal the structural information of the as-prepared PCNF–Co/N. The strong diffraction peaks centering at 44.4°, 51.9° and 76.2° are assigned to (111), (200) and (220) planes of metallic Co (PDF#15–0806) (Fig. 1b) [36,37], which was formed from in-situ reduction of Co^{2+} during the annealing process. The diffraction peak centering at 26° corresponds to the graphitic (002) plane. This diffraction peak is sharper than that of CNF because of a higher degree of graphitization by the catalytic function of Co metal [38]. Whereas, due to the volatility at high-temperature, no diffraction peak of metallic Zn was observed [39]. The pyrolysis of the self-assembled MOF along with the volatility of Zn should be responsible for the formation of highly porous structure. The surface area of PCNF–Co/N reached 69.26 m^2 g^{-1}, higher than CNF of 19.26 m^2 g^{-1} (Fig. 1c). The volumes of micropores smaller than 2 nm and mesopores in the range of 4–20 nm of PCNF–Co/N are increased significantly (Fig. 1d), which would benefit the penetration of Li$^+$-ion flux and reduce the surface energy of plated Li. Raman spectra indicate that both CNF and PCNF–Co/N show characteristic D (1345 cm^{-1}) and G bands (1580 cm^{-1}) of graphitic structure (Fig. S3) [36,40]. The intensity ratio of D to G band is 0.92 for CNF and 0.96 for PCNF–Co/N, indicating PCNF–Co/N possesses a higher degree

of disordered carbon that may result in enriched defects.

XPS was performed to reveal the bonding information on the surface. Prominent signals of C 1s, N 1s, O 1s and Co 2p are detected from the survey spectrum of PCNF–Co/N (Fig. 1e), whereas, there is no signal of Co existed in CNF (Fig. S4a). The Co 2p spectrum (Fig. 1f) shows a pair of typical Co 2p3/2 (782.6 eV)/Co 2p1/2 (796.2 eV) peaks, corresponding to the Co–Co bonds in metallic Co (779.8 eV) and the satellites (785.2 eV and 802.7 eV), respectively [37,41–44]. The N 1s peaks of both CNF (Fig. S4b) and PCNF–Co/N (Fig. 1g) are deconvoluted into PrN (C–NH–C, 400.5 eV), PyN (C=N–C, 398.3 eV), GrN (401.3 eV) and oxidized N (N–O, 402.0 eV), respectively [37,45,46]. The PrN and PyN occupy 46.4% of the total N in PCNF–Co/N, demonstrating a considerable increase compared with that of 25.3% in CNF (Table S1). ICP measurement suggests that the Co content in PCNF–Co/N is 62.33 mg g^{-1}.

SEM images reveal that CNF possess a uniform diameter of ca. 300 nm (Fig. 2a) and a wrinkled surface (Inset in Fig. 2a). Parallel hollow channels are in-situ created inside the CNF due to the sublimation of PMMA, as observed in the cross-sectional SEM image (Fig. 2b) and TEM image (Fig. 2b inset). The CNF film with a thickness of 40 ± 5 μm exhibits a robust and flexible texture (Fig. 2c). After immersing in the precursor solution of Co/Zn MOF, the interconnected 3D nanofibrous network is well-maintained (Fig. 2d). However, distinguished from pristine CNF with a clean surface, CNF@MOF nanofibers are covered thoroughly by uniformly arrayed nanosheets (Fig. 2e) without obvious
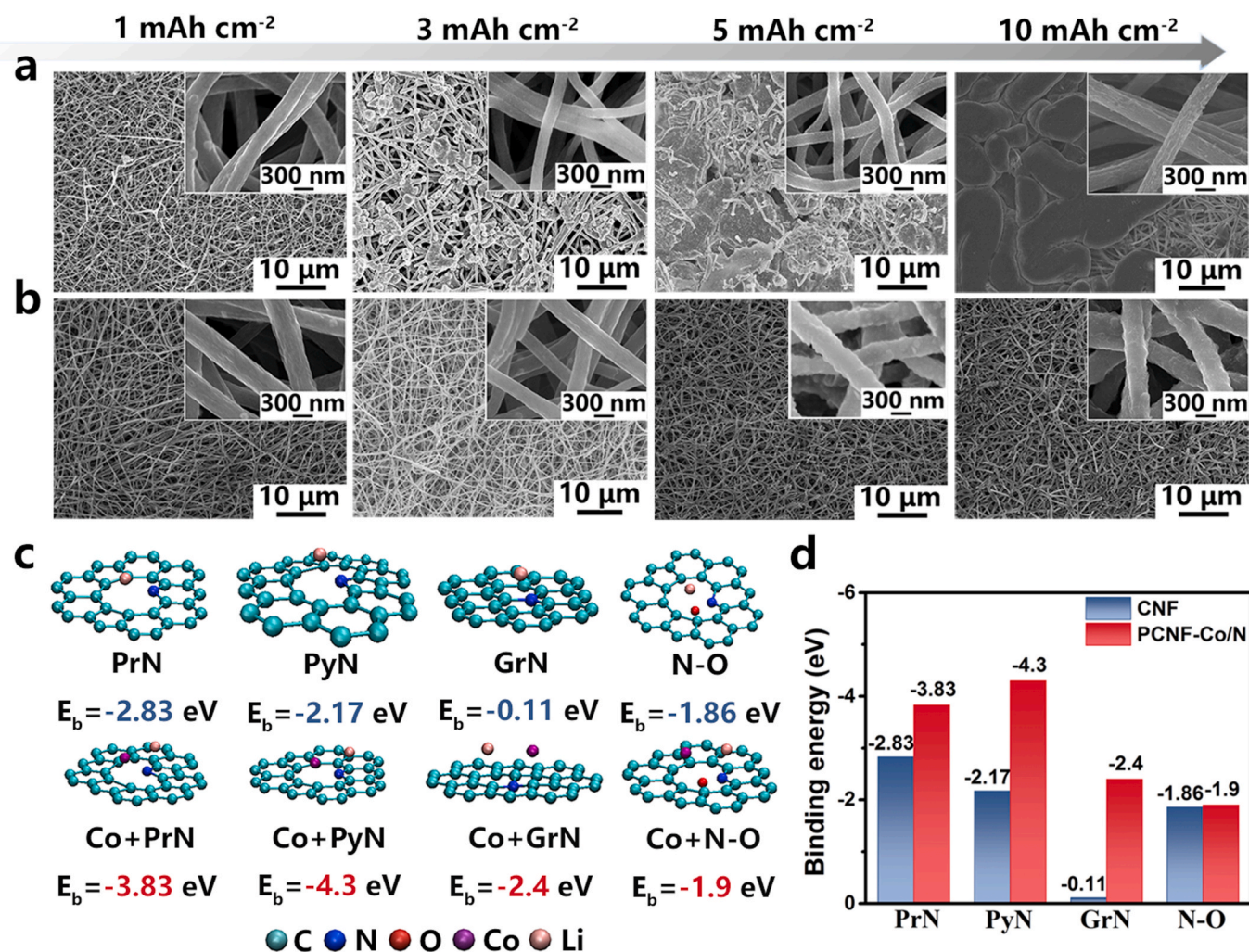
Fig. 4. SEM images of (a) CNF and (b) PCNF–Co/N deposited with different area capacity of Li at the current density of 0.5 mA cm^{-2}. (c) DFT calculation results of the interaction of a Li atom with PrN, PyN, GrN and *N*–O in CNF and PCNF–Co/N. (d) The corresponding binding energies.

change in thickness (Fig. 2f). After being calcined at 950 °C, the nanofibrous network could be still well-maintained (Fig. 2g). An etched porous surface (Fig. 2h) is observed on PCNF–Co/N nanofibers with similar thickness (Fig. 2i). Selected area electron diffraction (SAED) pattern of PCNF–Co/N exhibits distinct diffraction rings that could be indexed to (220), (200) and (111) planes of metallic Co (Fig. 2j) [46,47]. EDS analysis reveals the existence of C, N, O and Co elements that are distributed uniformly throughout the nanofibers (Fig. 2k–o).

3.2. Electrochemical characteristics of PCNF–Co/N nanofibers

The nucleation overpotential of Li plating is usually to evaluate the lithiophilicity of the substrate [30,48,49]. To investigate the Li metal plating process, electrochemical cells were assembled with a CNF, PCNF–Co/N or Cu foil as the working electrode and Li foil as the counter electrode. Under current density of 0.5 mA cm^{-2}, the nucleation overpotential of Li plating is only 11.2 mV for PCNF–Co/N, compared with 15.2 mV for CNF and 46 mV for Cu foil (Fig. 3a). During the initial discharge process, three voltage plateaus appear in the voltage profiles of CNF and PCNF–Co/N (Fig. S5a). The first two plateaus around 1.75 and 0.9 V vs. Li/Li$^+$ are from the parasitic reaction between Li$^+$ and C=N bonds to form Li–C–N–Li [44], and the Li adsorption into the porous structure of nanofibers, respectively [50]. The third plateau at ca. 0.1 V corresponds to the plating of Li at nucleation sites. The first and second plateaus disappear in following recharge and discharge,

suggesting a low reversible process. In accordance with the voltage profiles, CV profiles also show obvious peaks at 1.75, 0.9 and 0.1 V for both CNF and PCNF–Co/N nanofibers (Figs. S5b and c). The coulombic efficiency (CE) was measured for plating of 1 mAh cm^{-2} of Li and followed by stripping to 1.0 V (Fig. S6). For PCNF–Co/N electrode, the CE is 98.8% at 0.5 mA cm^{-2} for 200 cycles, compared with a deteriorate CE of CNF electrode after 150 cycles, and severe decayed CE of Cu electrode after 120 cycles (Fig. 3b). With current density increasing to 2 mA cm^{-2}, the PCNF–Co/N electrode still exhibits a stable CE above 96% for 150 cycles. In contrast, the CE of CNF and Cu electrodes show a quick drop after 70 and 50 cycles, respectively (Fig. 3c). These results suggest that better lithiophilicity and more stable electrode/electrolyte interface could be retained on PCNF–Co/N over prolonged cycling.

The stability of Cu@Li, CNF@Li or PCNF–Co/N@Li composite electrodes was evaluated by galvanostatic cycling in a symmetric cell. The electrodes were pre-deposited with 10 mAh cm^{-2} Li metal and tested at a fixed capacity of 1.0 mAh cm^{-2}. At a current density of 0.5 mA cm^{-2}, the PCNF–Co/N@Li electrode is highly stable for 1400 h (350 cycles) with small initial voltage hysteresis of ca. 4 mV (Fig. 3d). For CNF@Li electrode, sudden fluctuation occurs after cycling for 1200 h, and the initial voltage hysteresis is ca. 13 mV. For Cu@Li electrode, a sharp overpotential increase from ca. 45 mV to 100 mV is found in 110 h, probably caused by the internal short-circuit of fast Li dendrite growth [16,22]. When increasing the current density to 1 mA cm^{-2}, PCNF–Co/N@Li electrode exhibits a superior cycling stability over
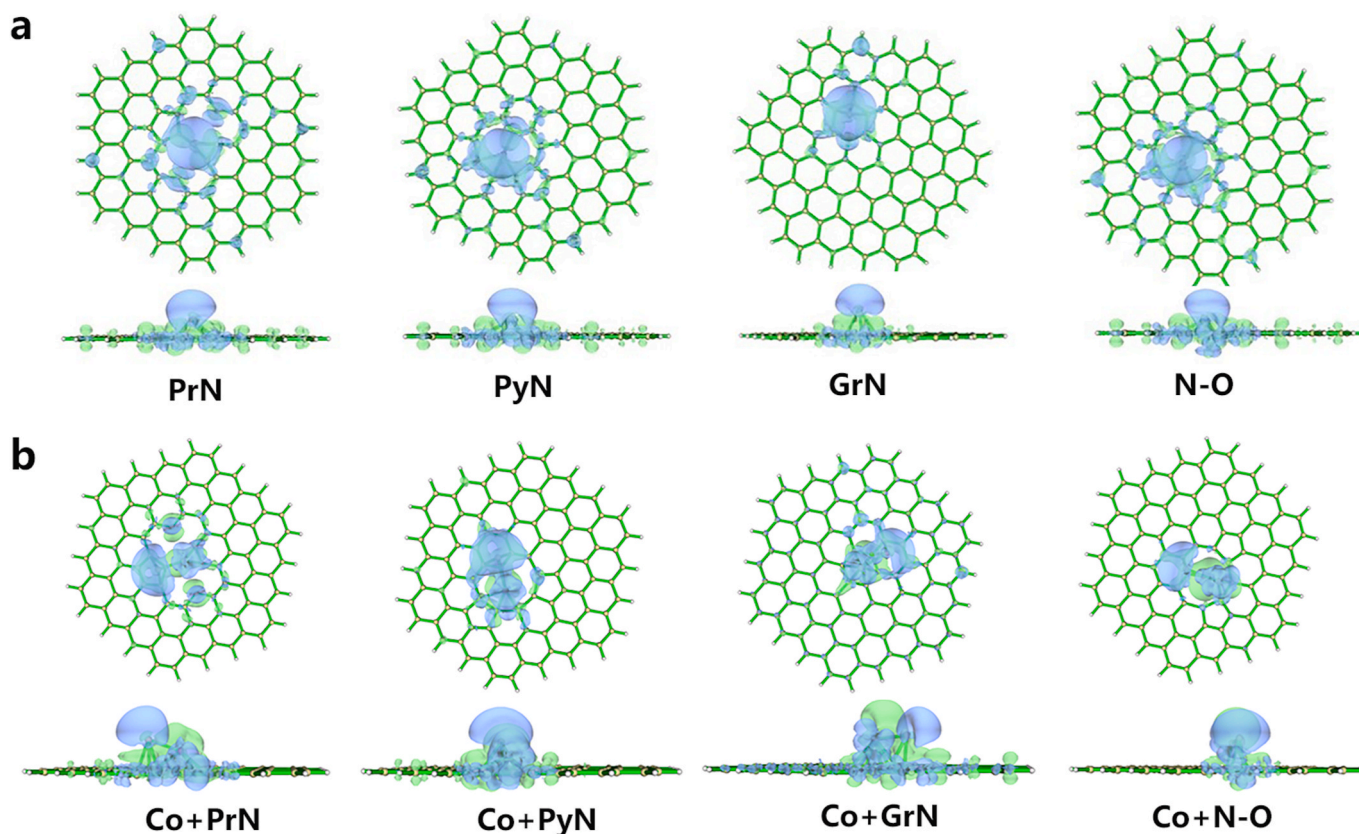
Fig. 5. The differential charge density at a Li atom adsorption site of PrN, PyN, GrN and *N*–O in (a) CNF and (b) PCNF–Co/N.

1100 h (550 cycles) with almost constant voltage hysteresis of ca. 14 mV. In comparison, CNF and Cu electrodes only survive for 700 and 200 h before short-circuit occurs (Fig. 3e). When further increasing the current density to 2 mA cm^{-2}, PCNF–Co/N@Li electrode still maintains good stability for 300 h (300 cycles) with slightly increased voltage hysteresis of ca. 24 mV (Fig. 3f). Even at a current density of 5 mA cm^{-2}, PCNF–Co/N could still stable for 60 h (150 cycles) (Fig. S7a). When fixing the cycling capacity to 2 mAh cm^{-2}, PCNF–Co/N could work smoothly over 600 h (150 cycles) at 1 mA cm^{-2} with a voltage hysteresis of ca. 19 mV (Fig. S7b). A comparison of PCNF–Co/N with the previously reported Li hosts suggests the electrochemical performance is among the top results of the symmetric cells (Table S2).

3.3. Electrochemical lithium plating/stripping mechanism

To reveal the origin of the cycling stability, morphological evolution of the electrodes during lithium plating/stripping processes was first investigated. For planar Cu, the Li strips scattered chaotically on the surface of copper at 1 mAh cm^{-2} and grow into bulks with the capacity increasing (Figs. S8a–e). Small Li nucleus formed near the intersections of the CNF nanofibers after Li plating for 1 mAh cm^{-2} (Fig. 4a). With discharge capacity gradually increasing to 10 mAh cm^{-2}, more and more Li metal deposits are formed on the surface of the CNF electrode. In contrast, the Li trends to nucleate homogeneously on individual fibers in the PCNF–Co/N electrode, and no Li deposit is found on the surface even with a discharge capacity of 10 mAh cm^{-2} (Fig. 4b). After sufficient Li stripping, large amounts of "dead Li" remains on the Cu foil (Fig. S8f) and some residual Li still exists in the interstices of the CNF (Figs. S9a and b), which is highly possible to serve as the uneven nucleation hotspots in next Li plating process. No residual Li deposits are observed on PCNF–Co/N film (Figs. S9c and d). The efficient Li plating/stripping on PCNF–Co/N probably due to the good Li affinity resulted from the highly

porous structure that alleviates the volume change, and the enriched lithiophilic PrN and PyN-like nitrogen defects that serve as the active sites for Li nucleation [24].

First-principle calculations were performed to reveal the origin of enriched lithiophilic nitrogen defects. For modeling, four optimized structures including PrN, PyN, GrN, and N–O according to XPS spectrum surveys were constructed (Fig. S10). N atoms exhibit relatively large electron affinity and possess lone pair electrons, Li atoms are therefore directly added on top of N in CNF (Fig. S11). Whereas in PCNF–Co/N, Co atoms are positively charged, which makes the local electrostatic potential (ESP) more complicate. To determine the best binding site for Li atom in PCNF–Co/N, we calculated the electrostatic potential for the PCNF–Co/N system and Li atom is added to the center of the positive ESP (Fig. S12).

The binding energy between Li atoms and N atoms in CNF and PCNF–Co/N was further calculated to clarify the synergistic effect of Co and N based on density functional theory (Fig. 4c). In the case of CNF, PrN (−2.83 eV), PyN (−2.16 eV) and N–O (−1.86 eV) show strong adsorption energy with Li, indicating these nitrogen defects are lithiophilic which lead to decreased nucleation overpotential and uniform Li plating. However, the binding energy of GrN with Li in CNF is only −0.11 eV, suggesting a weak interaction. In the case of PCNF–Co/N, the binding energy between Li and four kinds of N are more negative compared with those of CNF, indicating enhanced lithiophilic property when coordinated with Co. Notably, the binding energy of GrN with Li is −2.4 eV, proving its lithiophilic nature. The change of the binding energy could be more clearly distinguished in Fig. 4d. Moreover, the differential charge density analysis was also used to determine the charge transfer between Li and nitrogen sites (Fig. 5). The local charge density of Li with Co/N sites is obviously increased compared with pristine N, indicating the existence of a strong Li–Co/N interaction. The charge transfer result is in well accordance with binding energy. These
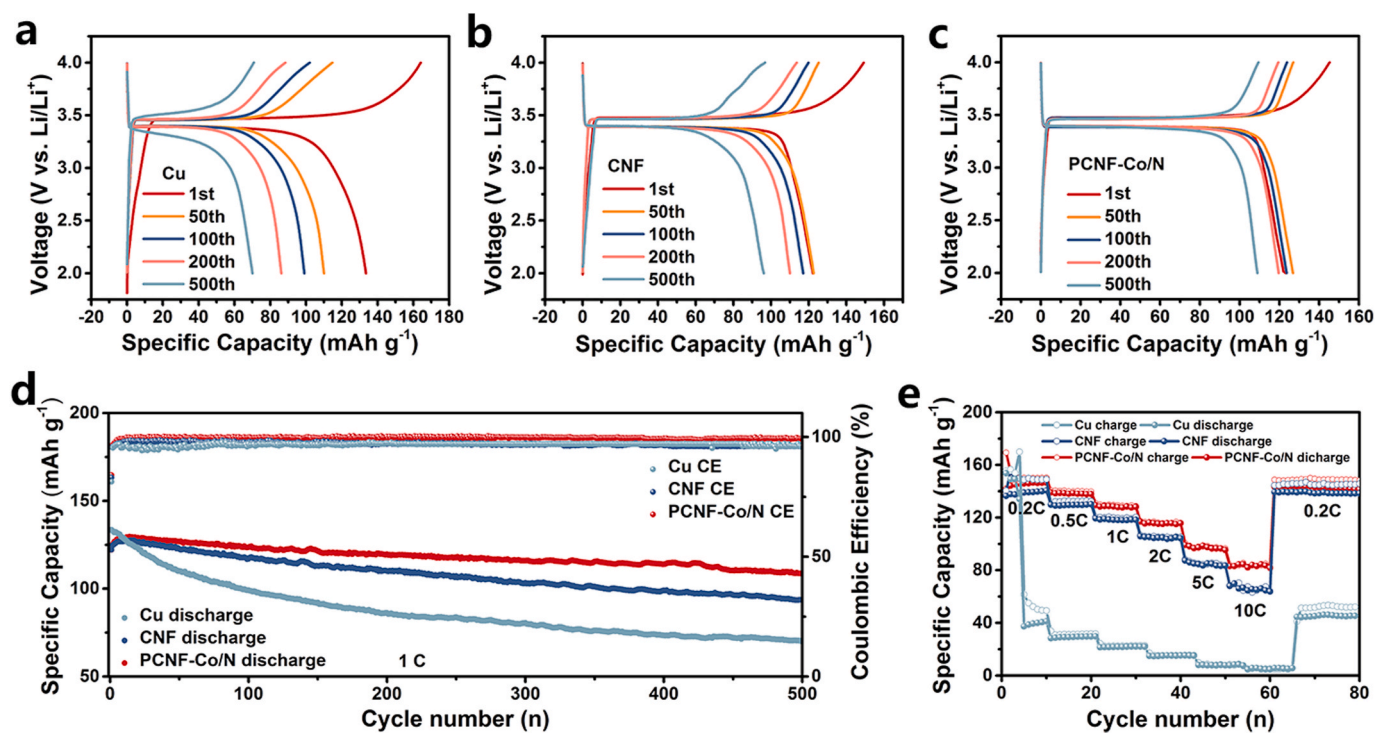
Fig. 6. Voltage-capacity profiles of (a) Cu@Li‖LiFePO₄, (b) CNF@Li‖LiFePO₄ and (c) PCNF–Co/N@Li‖LiFePO₄ cells at 1 C (1 C = 170 mA g⁻¹), and (d) corresponding cycling performance. (e) The corresponding rate performance.
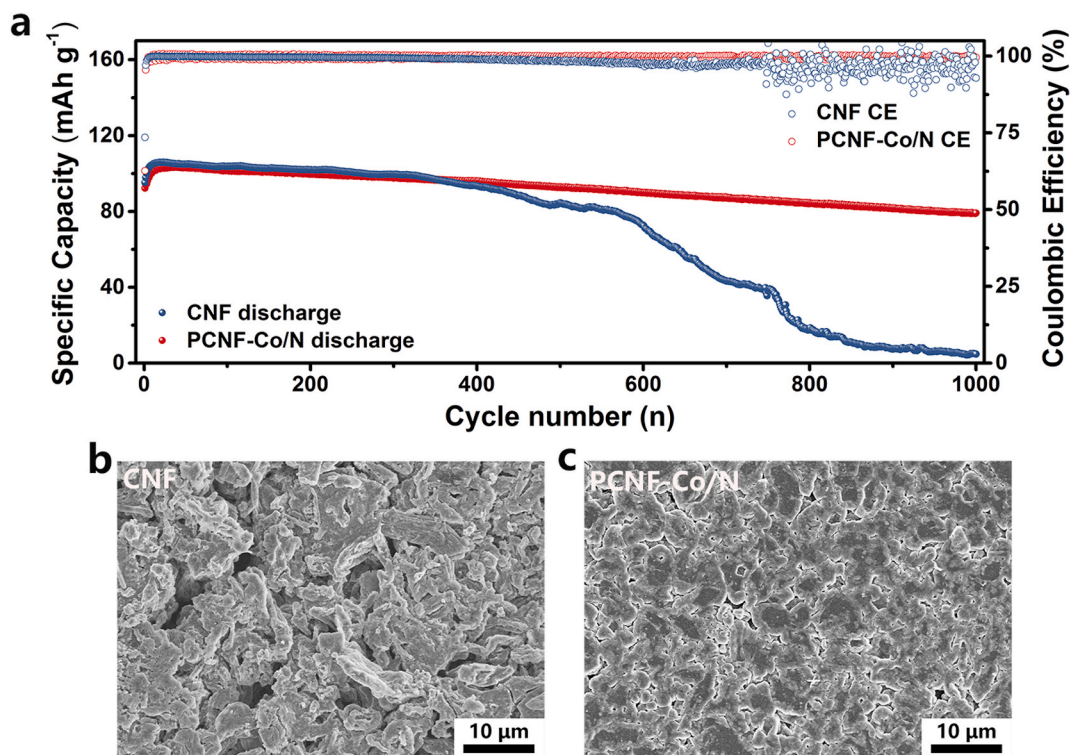

Fig. 7. (a) Cycling performance of CNF@Li‖LiFePO₄ and PCNF–Co/N@Li‖LiFePO₄ cells at 5 C. (b) SEM images of surface morphology of CNF@Li or (c) PCNF–Co/N@Li electrode after 1000 cycles.

calculation results suggests that the highly lithiophilic nature of nitrogen defects in PCNF–Co/N should be attributed to the synergistic effect of Co and N.

3.4. The performance of the cell with a LiFePO$_4$ cathode

To demonstrate the feasibility of PCNF–Co/N@Li anode for a practical cell, a commercial LiFePO$_4$ cathode was used to pair the Cu@Li, CNF@Li or PCNF–Co/N@Li anode. The galvanostatic voltage profiles at 1 C (1 C = 170 mA g^{-1}) represent the characteristic charge/discharge plateau of LiFePO$_4$ at ca. 3.45 V (vs. Li/Li$^+$) (Fig. 6a–c). The cell with PCNF–Co/N@Li delivers the highest discharge capacity of 122 mAh g^{-1} along with the highest CE of 89.1% in the first cycle. The capacity retention is 89% in the measured 500 cycles, corresponding to a decay of 0.02% per cycle (Fig. 6d). However, the CNF@Li or Cu@Li anode show a significant capacity decay of 23.6% and 47.6% within 500 cycles. Even at higher rates, the cell with PCNF–Co/N@Li delivers an obviously improved performance (Fig. 6e). For instance, the cell with PCNF–Co/N@Li anode still maintains a capacity of 92 mAh g^{-1} after 1000 cycles at 5 C, but the cell with CNF@Li anode deteriorates quickly after 400 cycles (Fig. 7a). Besides, dead Li deposits are obviously observed on the surface (Fig. 7b), whereas PCNF–Co/N@Li anode shows a clean surface (Fig. 7c), addressing its dendrite inhibition effects. EIS is further employed here to probe the interfacial charge transfer process at the electrode/electrolyte interface. The Nyquist plots of the cells before and after 500 cycles at 1 C along with the corresponding equivalent circuit are displayed in Fig. S13. Combined with the fitted parameters (Table S3), it is known that the fresh cell with a PCNF–Co/N@Li anode delivers a lower charge transfer resistance (R$_{ct}$) of 13.65 Ω compared to that with CNF@Li (19.88 Ω) and Cu@Li (40.75 Ω) anodes. After 500 cycles, the R$_{ct}$ of all cells decrease significantly and the R$_{ct}$ of that with PCNF–Co/N@Li (10.58 Ω) anode is still much lower than that of CNF@Li (17.35 Ω) and Cu@Li (21.38 Ω), suggesting a well-conductive passivation layer generated by reactions of Li and electrolytes are formed on the surface of PCNF–Co/N@Li nanofibers.

4. Conclusion

In summary, Co/N co-doped porous PCNF–Co/N was prepared through the pyrolysis of self-assembled MOF nanosheets on electrospun CNF. Owing to the enhanced Li affinity by the synergistic effect of Co/N coordination, the as-prepared PCNF–Co/N possesses a large amount of lithiophilic nitrogen defects like PrN, PyN, GrN and N–O, which all show strong adsorption with Li. The PCNF–Co/N with regular nucleation sites effectively guides the uniform plating/stripping of Li under high current densities. Moreover, the highly porous structure serves as a buffer to alleviate the internal stress of the nanofibers and reduces the local current density. As a result, a dendrite-free PCNF–Co/N@Li composite anode with a stable cyclability and good rate performance is realized in both symmetric and full cells. This work provides a feasible way to regulate Li plating/stripping behavior, which is highly desirable in high-energy Li metal batteries.

CRediT authorship contribution statement

Chengcheng Zhao: Investigation, Methodology, Writing - original draft, Writing - review & editing, Software, Visualization. **Shiyun Xiong:** Formal analysis, Methodology. **Huilan Li:** Data curation, Visualization. **Zhuhong Li:** Formal analysis, Investigation. **Chu Qi:** Data curation, Formal analysis. **Hao Yang:** Methodology, Conceptualization. **Lina Wang:** Methodology, Writing - original draft, Writing - review & editing, Visualization, Supervision, Funding acquisition. **Yu Zhao:** Writing - review & editing, Visualization, Supervision. **Tianxi Liu:** Supervision, Funding acquisition.

Declaration of competing interest

The authors declare that they have no known competing financial interests or personal relationships that could have appeared to influence the work reported in this paper.

Acknowledgements

Appendix A. Supplementary data

Supplementary data to this article can be found online at https://doi.org/10.1016/j.jpowsour.2020.229188.

References

[1] J.M. Tarascon, M. Armand, Issues and challenges facing rechargeable lithium batteries, Nature (Lond.) 414 (2001) 359–367.
[2] C.P. Yang, Y.X. Yin, S.F. Zhang, N.W. Li, Y.G. Guo, Accommodating lithium into 3D current collectors with a submicron skeleton towards long-life lithium metal anodes, Nat. Commun. 6 (2015) 8058–8067.
[3] L. Chen, X. Fan, X. Ji, J. Chen, S. Hou, C.S. Wang, High-energy Li metal battery with lithiated host, Joule 3 (2019) 732–745.
[4] P.G. Bruce, S.A. Freunberger, L.J. Hardwick, J.M. Tarascon, Li–O$_2$ and Li–S batteries with high energy storage, Nat. Mater. 11 (2011) 19–29.
[5] D. Lin, Y. Liu, Y. Cui, Reviving the lithium metal anode for high-energy batteries, Nat. Nanotechnol. 12 (2017) 194–206.
[6] Y. Guo, H. Li, T. Zhai, Reviving lithium-metal anodes for next-generation high-energy batteries, Adv. Mater. 29 (2017) 1700007.
[7] W. Xu, J. Wang, F. Ding, X. Chen, E. Nasybulin, Y. Zhang, J.G. Zhang, Lithium metal anodes for rechargeable batteries, Energy Environ. Sci. 7 (2014) 513–537.
[8] J. Zheng, M.H. Engelhard, D. Mei, S. Jiao, B.J. Polzin, J.G. Zhang, W. Xu, Electrolyte additive enabled fast charging and stable cycling lithium metal batteries, Nat. Energy 2 (2017) 17012.
[9] W. Deng, W. Zhu, X. Zhou, X. Peng, Z. Liu, Highly reversible Li plating confined in three-dimensional interconnected microchannels toward high-rate and stable metallic lithium anodes, ACS Appl. Mater. Interfaces 10 (2018) 20387–20395.
[10] Y. Lu, Z. Tu, L.A. Archer, Stable lithium electrodeposition in liquid and nanoporous solid electrolytes, Nat. Mater. 13 (2014) 961–969.
[11] C. Yan, Y. Yao, X. Chen, X. Cheng, X. Zhang, J. Huang, Q. Zhang, Lithium nitrate solvation chemistry in carbonate electrolyte sustains high-voltage lithium metal batteries, Angew Chem. Int. Ed. Engl. 130 (2018) 14251–14255.
[12] X. Shen, X. Li, T. Qian, J. Liu, J. Zhou, C. Yan, J.B. Goodenough, Lithium anode stable in air for low-cost fabrication of a dendrite-free lithium battery, Nat. Commun. 10 (2019) 900–909.
[13] P. Li, X. Dong, C. Li, J. Liu, Y. Liu, W. Feng, C. Wang, Y. Wang, Y. Xia, Anchoring an artificial solid-electrolyte interphase layer on a 3D current collector for high-performance lithium anodes, Angew Chem. Int. Ed. Engl. 58 (2019) 2093–2097.
[14] G. Zheng, S.W. Lee, Z. Liang, H.W. Lee, K. Yan, H. Yao, H. Wang, W. Li, S. Chu, Y. Cui, Interconnected hollow carbon nanospheres for stable lithium metal anodes, Nat. Nanotechnol. 9 (2014) 618–623.
[15] Q. Li, S. Zhu, Y. Lu, 3D porous Cu current collector/Li-metal composite anode for stable lithium-metal batteries, Adv. Funct. Mater. 27 (2017) 1606422.
[16] Y. He, H. Xu, J. Shi, P. Liu, Z. Tian, N. Dong, K. Luo, X. Zhou, Z. Liu, Polydopamine coating layer modified current collector for dendrite-free Li metal anode, Energy Storage Mater 23 (2019) 418–426.
[17] L.L. Lu, J. Ge, J.N. Yang, S.M. Chen, H.B. Yao, F. Zhou, S.H. Yu, Free-standing copper nanowire network current collector for improving lithium anode performance, Nano Lett. 16 (2016) 4431–4437.
[18] C. Brissot, M. Rosso, C.J. N, P. Baudry, S. Lascaud, In situ study of dendritic growth in lithium/PEO-salt/lithium cells, Electrochim. Acta 43 (1998) 1569–1574.
[19] H. Ye, S. Xin, Y. Yin, Y. Guo, Advanced porous carbon materials for high-efficient lithium metal anodes, Adv. Energy Mater. 7 (2017) 1700530.
[20] Q. Yun, Y. He, W. Lv, Y. Zhao, B. Li, F. Kang, Q. Yang, Chemical dealloying derived 3D porous current collector for Li metal anodes, Adv. Mater. 28 (2016) 6932.
[21] X.B. Cheng, H.J. Peng, J.Q. Huang, R. Zhang, C.Z. Zhao, Q. Zhang, Dual-phase lithium metal anode containing a polysulfide-induced solid electrolyte interphase and nanostructured graphene framework for lithium-sulfur batteries, ACS Nano 9 (2015) 6373–6382.
[22] T.T. Zuo, X.W. Wu, C.P. Yang, Y.X. Yin, H. Ye, N.W. Li, Y.G. Guo, Graphitized carbon fibers as multifunctional 3D current collectors for high areal capacity Li anodes, Adv. Mater. 29 (2017) 1700389.
[23] Y. Yang, M. Zhao, H. Geng, Y. Zhang, Y. Fang, C. Li, J. Zhao, Three-dimensional graphene/Ag aerogel for durable and stable Li metal anodes in carbonate-based electrolytes, Chemistry 25 (2019) 5036–5043.

[24] R. Zhang, X.R. Chen, X. Chen, X.B. Cheng, X.Q. Zhang, C. Yan, Q. Zhang, Lithiophilic sites in doped graphene guide uniform lithium nucleation for dendrite-free lithium metal anodes, Angew Chem. Int. Ed. Engl. 56 (2017) 7764–7768.

[25] K. Yan, Z. Lu, H.W. Lee, F. Xiong, P.C. Hsu, Y. Li, J. Zhao, S. Chu, Y. Cui, Selective deposition and stable encapsulation of lithium through heterogeneous seeded growth, Nat. Energy 1 (2016) 16010–16017.

[26] H. Wang, Y. Li, Y. Li, Y. Liu, D. Lin, C. Zhu, G. Chen, A. Yang, K. Yan, H. Chen, Y. Zhu, J. Li, J. Xie, J. Xu, Z. Zhang, R. Vila, A. Pei, K. Wang, Y. Cui, Wrinkled graphene cages as hosts for high capacity Li metal anodes shown by cryogenic electron microscopy, Nano Lett. 19 (2019) 1326–1335.

[27] X.Y. Yue, W.W. Wang, Q.C. Wang, J.K. Meng, X.X. Wang, Y. Song, Z.W. Fu, X. J. Wu, Y.N. Zhou, Cuprite-coated Cu foam skeleton host enabling lateral growth of lithium dendrites for advanced Li metal batteries, Energy Storage Mater 21 (2019) 180–189.

[28] J.Y. Kim, G. Liu, M.X. Tran, R.E. Anugrah Ardhi, H. Kim, J.K. Lee, Synthesis and characterization of a hierarchically structured three-dimensional conducting scaffold for highly stable Li metal anodes, J. Mater. Chem. A. 7 (2019) 12882–12892.

[29] X. Ke, Y. Liang, L. Ou, H. Liu, Y. Chen, W. Wu, Y. Cheng, Z. Guo, Y. Lai, P. Liu, Z. Shi, Surface engineering of commercial Ni foams for stable Li metal anodes, Energy Storage Mater 23 (2019) 547–555.

[30] P. Xue, S. Liu, X. Shi, C. Sun, C. Lai, Y. Zhou, D. Sui, Y. Chen, J. Liang, A hierarchical silver-nanowire–graphene host enabling ultrahigh rates and superior long-term cycling of lithium-metal composite anodes, Adv. Mater. 30 (2018) 1804165.

[31] S. Li, Q. Liu, J. Zhou, T. Pan, L. Gao, W. Zhang, L. Fan, Y. Lu, Hierarchical Co3O4 nanofiber–carbon sheet skeleton with superior Na/Li-philic property enabling highly stable Alkali metal batteries, Adv. Funct. Mater. 29 (2019) 1808847.

[32] T. Wang, P. Zhai, D. Legut, L. Wang, X. Liu, B. Li, C. Dong, Y. Fan, Y. Gong, Q. Zhang, S-doped graphene-regional nucleation mechanism for dendrite-free lithium metal anodes, Adv. Energy Mater. 9 (2019) 1804000.

[33] M.J. Frisch, G.W. Trucks, H.B. Schlegel, G.E. Scuseria, M.A. Robb, J.R. Cheeseman, G. Scalmani, V. Barone, B. Mennucci, G.A. Petersson, H. Nakatsuji, M. Caricato, X. Li, H.P. Hratchian, A.F. Izmaylov, J. Bloino, G. Zheng, J.L. Sonnenberg, M. Hada, M. Ehara, K. Toyota, R. Fukuda, J. Hasegawa, M. Ishida, T. Nakajima, Y. Honda, O. Kitao, H. Nakai, T. Vreven, J.A. Montgomery Jr., J.E. Peralta, F. Ogliaro, M. Bearpark, J.J. Heyd, E. Brothers, K.N. Kudin, V.N. Staroverov, R. Kobayashi, J. Normand, K. Raghavachari, A. Rendell, J.C. Burant, S.S. Iyengar, J. Tomasi, M. Cossi, N. Rega, J.M. Millam, M. Klene, J.E. Knox, J.B. Cross, V. Bakken, C. Adamo, J. Jaramillo, R. Gomperts, R.E. Stratmann, O. Yazyev, A.J. Austin, R. Cammi, C. Pomelli, J.W. Ochterski, R.L. Martin, K. Morokuma, V.G. Zakrzewski, G.A. Voth, P. Salvador, J.J. Dannenberg, S. Dapprich, A.D. Daniels, Ö. Farkas, J. B. Foresman, J.V. Ortiz, J. Cioslowski, D.J. Fox, Gaussian 09, Revision D.01, Gaussian Inc., Wallingford, CT, 2009.

[34] T. Lu, F. Chen, Multiwfn: a multifunctional wavefunction analyzer, J. Comput. Chem. 33 (2012) 580.

[35] N. Abeykoon, J. Bonso, J. Ferraris, Supercapacitor performance of carbon nanofiber electrodes derived from immiscible PAN/PMMA polymer blends, RSC Adv. 5 (2015) 19865–19873.

[36] G. Li, W. Lei, D. Luo, Y. Deng, Z. Deng, D. Wang, A. Yu, Z. Chen, Stringed "tube on cube" nanohybrids as compact cathode matrix for high-loading and lean-electrolyte lithium-sulfur batteries, Energy Environ. Sci. 11 (2018) 2372–2381.

[37] S. Chen, Y. Zheng, B. Zhang, Y. Feng, J. Zhu, J. Xu, C. Zhang, W. Feng, T. Liu, Cobalt, nitrogen-doped porous carbon nanosheet-assembled flowers from metal-coordinated covalent organic polymers for efficient oxygen reduction, ACS Appl. Mater. Interfaces 11 (2019) 1384–1393.

[38] J. Tang, R. Salunkhe, H. Zhang, V. Malgras, T. Ahamad, S. Alshehri, N. Kobayashi, S. Tominaka, Y. Ide, J. Kim, Y. Yamauchi, Bimetallic metal-organic frameworks for controlled catalytic graphitization of nanoporous carbons, Sci. Rep. 6 (2016) 30295–30302.

[39] D. Xu, D. Chao, H. Wang, Y. Gong, R. Wang, B. He, X. Hu, H.J. Fan, Flexible quasi-solid-state sodium-ion capacitors developed using 2D metal-organic-framework array as reactor, Adv. Energy Mater. 8 (2018) 1702769.

[40] fish 0,punct]">F. Zheng, Y. Yang, Q. Chen, High lithium anodic performance of highly nitrogen-doped porous carbon prepared from a metal-organic framework, Nat. Commun. 5 (2014) 5261–5270.

[41] J. Meng, C. Niu, L. Xu, J. Li, X. Liu, X. Wang, Y. Wu, X. Xu, W. Chen, Q. Li, Z. Zhu, D. Zhao, L. Mai, General oriented formation of carbon nanotubes from metal-organic frameworks, J. Am. Chem. Soc. 139 (2017) 8212–8221.

[42] S.K. Park, J.K. Lee, Y.C. Kang, Yolk-shell structured assembly of bamboo-like nitrogen-doped carbon nanotubes embedded with Co nanocrystals and their application as cathode material for Li–S batteries, Adv. Funct. Mater. 28 (2018) 1705264.

[43] X. Liu, Y. Wang, Z. Wang, T. Zhou, M. Yu, L. Xiu, J. Qiu, Achieving ultralong life sodium storage in amorphous cobalt-tin binary sulfide nanoboxes sheathed in N-doped carbon, J. Mater. Chem. 5 (2017) 10398–10405.

[44] C. Su, H. Cheng, W. Li, Z. Liu, N. Li, Z. Hou, F. Bai, H. Zhang, T. Ma, Atomic modulation of FeCo-Nitrogen-Carbon bifunctional oxygen electrodes for rechargeable and flexible all-solid-state zinc-air battery, Adv. Energy Mater. 7 (2017) 1602420.

[45] X. Wang, Y. Qian, L. Wang, H. Yang, H. Li, Y. Zhao, T. Liu, Sulfurized polyacrylonitrile cathodes with high compatibility in both ether and carbonate electrolytes for ultrastable lithium-sulfur batteries, Adv. Funct. Mater. 29 (2019) 1902929.

[46] W. Cai, G. Li, D. Luo, G. Xiao, S. Zhu, Y. Zhao, Z. Chen, Y. Zhu, Y. Qian, The dual-play of 3D conductive scaffold embedded with Co, N codoped hollow polyhedra toward high-performance Li–S full cell, Adv. Energy Mater. 8 (2018) 1802561.

[47] Y. Zhao, Q. Lai, J. Zhu, J. Zhong, Z. Tang, Y. Luo, Y. Liang, Controllable construction of core-shell Polymer@Zeolitic imidazolate frameworks fiber derived heteroatom-doped carbon nanofiber network for efficient oxygen electrocatalysis, Small 14 (2018) 1704207.

[48] S. Huang, W. Zhang, H. Ming, G. Cao, L.Z. Fan, H. Zhang, Chemical energy release driven lithiophilic layer on 1 m^2 commercial brass mesh toward highly stable lithium metal batteries, Nano Lett. 19 (2019) 1832–1837.

[49] A. Pei, G. Zheng, F. Shi, Y. Li, Y. Cui, Nanoscale nucleation and growth of electrodeposited lithium metal, Nano Lett. 17 (2017) 1132–1139.

[50] G. Yang, X. Li, Z. Guan, Y. Tong, B. Xin, X. Wang, Z. Wang, L. Chen, Insights into lithium and sodium storage in porous carbon, Nano Lett. (2020), https://doi.org/10.1021/acs.nanolett.0c00943.